Materials Today Nano 21 (2023) 100303

Contents lists available at ScienceDirect

Materials Today Nano

journal homepage: https://www.evise.com/profile/#/MTNANO/login

Chiral metal-organic framework based spin-polarized flexible photodetector with ultrahigh sensitivity

M. Mustaqeem [a, b, c, **], S. Kamal [d], N. Ahmad [e], P.-T. Chou [a], K.-H. Lin [f], Y.-C. Huang [g], G.-Y. Guo [b], C.R. Paul Inbaraj [b], W.-K. Li [b], H.-C. Yao [f], K.-L. Lu [d, ***], Y.-F. Chen [b, *]

[a] Department of Chemistry, National Taiwan University, No. 1, Section 4, Roosevelt Rd, Taipei, 10617
[b] Department of Physics, National Taiwan University, No. 1, Section 4, Roosevelt Rd, Taipei, 10617
[c] Nano-Science and Technology Program, Taiwan International Graduate Program, Institute of Physics, Academia Sinica, Taipei, 106, Taiwan
[d] Institute of Chemistry, Academia Sinica, Taipei, 115, Taiwan
[e] Department of Materials Science and Engineering, National Taiwan University of Science and Technology, Taipei, 10607, Taiwan
[f] Institute of Physics, Academia Sinica, Taipei, 11529 Taiwan
[g] Department of Materials Engineering, Ming Chi University of Technology

ARTICLE INFO

Article history:
Received 19 September 2022
Received in revised form
29 November 2022
Accepted 3 January 2023
Available online 6 January 2023

Keywords:
Spin-photodetector
Anisotropy factor (g_{lph})
Chiral Metal- Organic Network , Spin-optoelectronics

ABSTRACT

Spin-optoelectronics plays a key role in developing next-generation technologies with potential applications covering from pharmaceutical synthesis and quantum computing to optical communication. One of the most feasible ways to achieve high-performance spin optoelectronic devices is based on chiral materials. Chiral metal-organic frameworks (CMOFs), an emerging class of chiral hybrid materials, have sparked interest due to their structural variety and flexibility, order nanopores, cost-effectiveness, and unique chirality features. Herein, we have developed CMOF [Sr (9,10-adc) $(DMAc)_2]_n$ based on achiral building blocks [(9,10-adc)] to detect circularly polarized light (CPL) with ultrahigh sensitivity. Their application in spin-polarized flexible detectors gives a detectivity (D*) as high as 1.83×10^{12} jones, superior to all reported heterochiral MOF-based detectors. Meanwhile, the anisotropy factor (g_{lph}) is up to 0.38 for CPL detection. The maximum photoresponsivity (R_{ph}) and photogain (η) values of CMOFs reach up to 6.0×10^5 (A/W) and 1.8×10^6, respectively, which are also the record values among reported chiral MOFs. Additionally, the photodetector is mechanically flexible and durable, manifesting an important feature for wearable devices. Therefore, our study shown here is significant and timely to open a route for advancing spin-optoelectronics based on CMOF.

1. Introduction

Spin-optoelectronics uses unpolarized or circular polarized light (CPL) to interact with electron spin, generating corresponding devices for practical applications. Many optoelectronic technologies are attentive to CPL, such as circular polarization ellipsometry-based tomographic scanning, spin information and optical communication, and quantum-based optical computation and data processing. Achieving circularly polarized photon states is critical to spin information processing in monitoring photons' and electronic spins' interactions [1–3]. One of the most efficient methodologies to obtain high performance spin optoelectronic devices is to implement chiral materials as the active layer. Therefore, the advancement of chiral materials has captivated a lot of consideration, owing to their practical benefits in agricultural production [4] and pharmaceutical synthesis [5], in addition to their applications in optoelectronic devices [6–10]. Chiral materials distinguished from mirror copies display nonlinear optical reactions to CPL. An electric vector of constant magnitude spins with a constant angular velocity in a plane perpendicular to the propagation direction. In chiral materials, the incoming left-handed circularly polarized light (LCPL) or right-handed circularly polarized light (RCPL), i.e., circular dichroism (CD), can produce a differential circulation of electronic charges, resulting in varying degrees of light absorption [11]. Chiral organic compounds, for instance, have been used in the direct CPL detection systems, using

* Corresponding author.
** Corresponding author.
*** Corresponding author.
E-mail addresses: d09223113@ntu.edu.tw (M. Mustaqeem), kllu@gate.sinica.edu.tw (K.-L. Lu), yfchen@phys.ntu.edu.tw (Y.-F. Chen).

https://doi.org/10.1016/j.mtnano.2023.100303
2588-8420/

their inherent chiral sensitivity [12]. Note that photodetector is one of the indispensable key components for the application of spin optoelectronic devices. Generally, the photodetectors made with organic compounds often show low responsivity due to low exciton dissociation energy and poor charge carrier mobility, limiting their practical uses for sensitive CPL detection. Thus, high-performance CPL detection prerequisites the development of both CPL-sensitive and photoactive materials with excellent charge carrier characteristics.

Chiral metal-organic frameworks (CMOFs), a developing class of chiral hybrid materials, have sparked much interest due to their structural variety, order nanopores, and unique chirality features. CMOFs have played a vital role in numerous research areas, such as asymmetric catalysis, sensing, nonlinear optics, and optical device [13–16]. Scientists recently discovered that employing CMOFs to produce CPL materials offered a viable approach. Chirality in CMOFs can occur due to an asymmetric environment, chiral agents in precursors, or even specialized configurations of achiral precursors that result in spontaneous resolution. CMOFs were developed in a non-centrosymmetric space group, which lacked inversion symmetry. As a result of the lack of a local inversion centre, a dominating intensity was observed in these types of MOFs' f–f transitions. Thus, analyzing this intensity in conjunction with the crystal structure enables to demonstrate the establishment of a chiral environment surrounding the rare earth ions within complexes [17,18]. Even though a wide range of materials has lately been explored for the application in photodetectors, however, to the best of our knowledge, research investigations on the performance of CMOF-based spin photodetectors are still rather limited since most CMOFs have low conductivity and are too massive to be used in optoelectronic devices. In particular, the synthesized Sr-based CMOFs for CPL detection have not been reported, even though they might be attractive candidates in practical spin optoelectronic applications for their unique feature of chirality and order porous structure for light trapping.

Herein, we have developed CMOFs based on achiral building blocks to serve as a highly efficient spin-polarized flexible photodetector. The single-crystal X-ray diffraction confirmed the tetragonal space group *I -4 2 d,* and powder X-ray diffraction (PXRD) are in good accordance with the simulation results. The non-centrosymmetric chiral space group, *I -4 2 d,* shows second harmonic generation (SHG) and an excellent nonlinear optical (NLO) response. Chiral centers indicate SHG in a donor-acceptor system, which leads to a greater hyperpolarizability. Grazing incidence wide-angle X-ray scattering (GIWAXS) data suggests the highly crystalline and ordered CMOFs film. The maximum photoresponsivity (R_{ph}), photogain (η), and detectivity (D*) values of CMOFs were 6.0×10^5 (A/W), $1.8 \times 10^{6,}$ and 1.83×10^{12} jones, respectively, under an applied bias of 0.1 V and 405 nm irradiation. The resulting detectivity and photoresponsivity are higher than all the reported heterochiral MOFs-based photodetectors [19]. This CPL detector has excellent distinguishability with a spin photocurrent anisotropy factor (g_{Iph}) of 0.38, which can be attributed to the extended spin lifetimes in highly crystalline CMOFs. In the current designed device structure, CMOFs/graphene heterojunction plays a crucial role, where the porous morphology of CMOFs is able to produce a light-trapping effect to enhance light harvesting and generate more electron-hole pairs. The generated charges enable transferring to the graphene layer, drastically increasing the photocurrent due to the high carrier mobility of graphene. Because each constituent material in the as prepared device is bendable, the photodetector is mechanically flexible and durable, which is an important feature for wearable devices. Our findings of achieving high-performance and flexible spin photodetector based on CMOFs thus pave a key step to open a useful approach for developing future spin optoelectronic devices.

2. Results and discussion

[Sr (9,10-adc) $(DMAc)_2$]n (CMOF) were prepared by the hydrothermal reaction of 9,10-anthracene dicarboxylic acid [(9,10-adc)] with $Sr(NO)_3$ in a solvent mixture of DMAc and H_2O at 140 °C (Scheme 2). A single-crystal X-ray diffraction study indicated that CMOF crystallizes in the tetragonal space group I –4 2 d (Table S1, Supplementary Information). The asymmetric unit of CMOF (Fig. 1a) consists of a Sr(II) centre, adc^{2-} ligand, and DMAc molecules. The Sr(II) centre coordinates with four distinct adc^{2-} ligands in a monodentate fashion while with one adc^{2-} and two dmac molecules in a bidentate manner through their carboxylate ends (O2, O2') and (O3, O3') respectively, giving rise to an octahedral geometry (Fig. 1a). Two neighboring Sr (II) centers are linked by the O1and O2 atoms contributing to an adc^{2-} ligand, forming one-dimensional metal oxide chains composed of building units. The Sr···Sr distance in this 1D chain is 4.00 Å, and the Sr–O bond length ranges from 2.68 Å to 2.56 Å. One dimensional Sr–O–Sr chains in 1 are pillared by adc^{2-} ligands on each side and extend outwards to form a layered 3D network (Fig. 1b). When viewed along the b axis, the distance between two individual 1D chains is about 10.2–14.0 Å (Fig. 1c).

The powder X-ray diffraction (PXRD) data were collected to confirm the purity of CMOF. The peak positions of the experimental PXRD patterns are in good agreement with simulated findings generated using single-crystal data, ensuring the excellent purity of the synthesized materials. The discrepancy in reflection intensities between the simulated and experimental configurations can be attributed to variations in the randomly oriented powder samples during the experimental PXRD data collection (Fig. 2a). The morphology of CMOF was characterized by field emission scanning electron microscopy (FESEM), as shown in Fig. S1a. It depicts that the CMOF presents a rectangular morphology with varying sizes of crystals. The energy dispersive spectroscopy (EDS) point scanning (Fig. S1b, Supplementary Information), as well as elemental mapping images of CMOF (Fig. S1c), were collected to investigate the chemical composition and elemental distribution of CMOF. The findings further evidence that C, O, and Sr elements exist in CMOF. TGA evaluated the thermal stability of CMOF. As shown in Fig. 2b, a sample comprising several single crystals was heated in an N_2 atmosphere at a heating rate of 10 °C/min. The Figure shows that CMOF is stable up to 160 °C, and 2.5% weight loss at 160–193 °C corresponds to the loss of guest water molecules. The 15.6% weight loss in the 260–330 °C occurs owing to coordinated dimethylacetamide molecules decomposition, and 2,9-anthracene occurs in the temperature range of 330–450 °C.

CMOF was crystallized in the non-centrosymmetric chiral space group (I –4 2d), and its SHG characteristics and interaction were compared to silica, a reference material. The findings of the experiments demonstrated that the crystal CMOF sample displayed intense SHG activity, with a reactivity 40 times larger than that of silica (Fig. 2c). The increased SHG activity can be linked to chiral centers within a donor-acceptor system, which leads to the enhanced hyperpolarizability. CMOF's structured organic fluorophores are compatible with the single-crystal data and have strong π–π stackings. The free ligand, on the other hand, did not exhibit any SHG response. Our strategy of using a highly conjugated ligand to create a multilayer 3D network with asymmetrical coordination (chelating and monodentate carboxylate modes on either side) towards Sr metal centers was highly successful. It finally exhibits a chiral structure with a chiral space group. In addition, it is

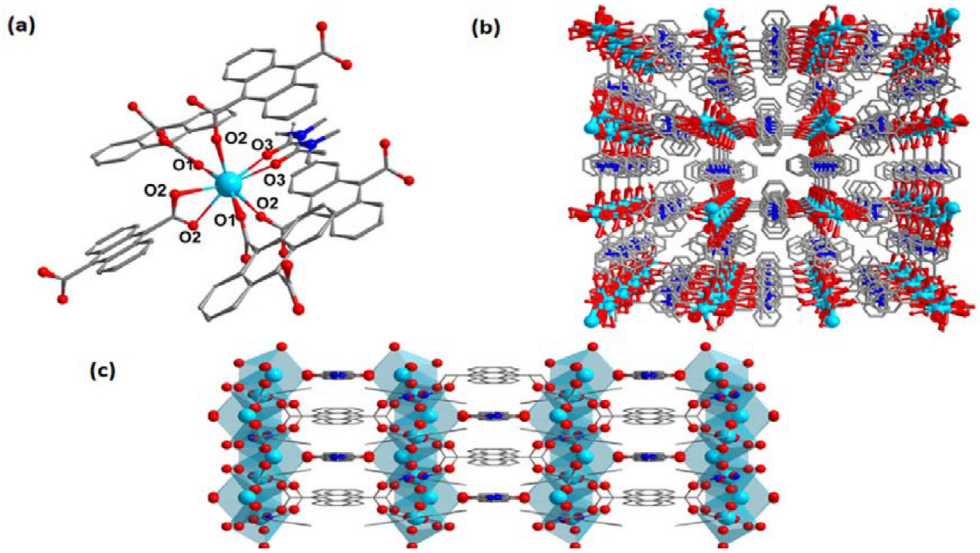

Fig. 1. (a) Coordination environment of the Sr metal centre in 1. (b) 3D structure of compound 1(c) adc^{2-} ligand bridged between metal-oxygen (M – O) chains.

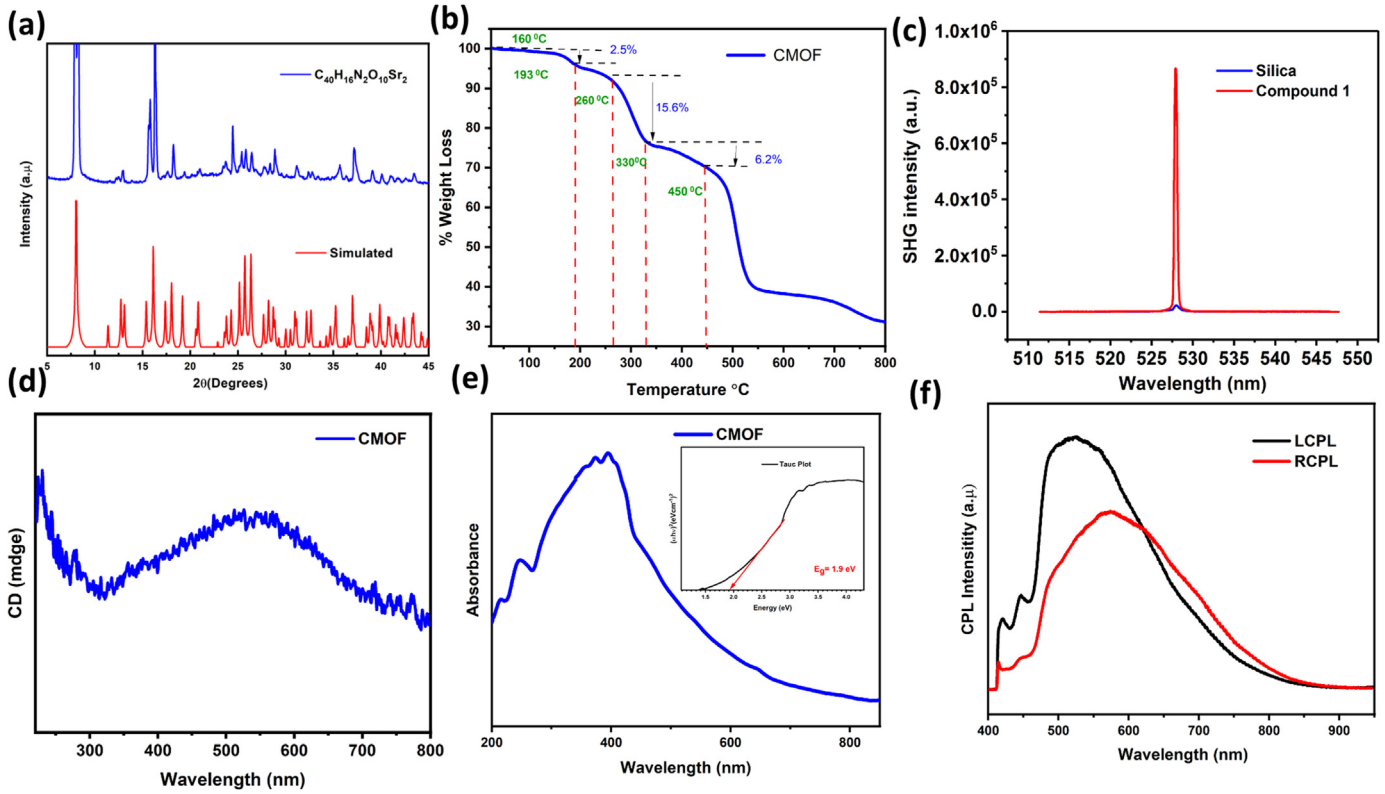

Fig. 2. (a) Shows the as-synthesized and simulated PXRD patterns for CMOF. (b) Thermogravimetric analysis curve for CMOF as a function of temperature. (c) SHG spectra of CMOF crystals excited by a pulsed Q-switched Nd-YAG laser at 1064 nm. (d) CD spectra of CMOF. (e) UV–vis absorption spectra of CMOF and the inserted graph is Tauc plot. (f) PL spectra of CMOF under the CPL illumination of 405 nm laser.

also worth mentioning that the presence of an achiral ligand achieves the MOF structure's chirality.

The chirality of the CMOF is also further confirmed via CD spectra (Fig. 2d). CD spectra have shown the cotton effect at 320 nm and 530 nm, respectively. The result proves that the chirality of MOF is directly transferred from the achiral ligand [20]. To evaluate the artifacts in CD, we measured linear dichroism (LD) spectra of the CMOF using the reported method [21]. The LD spectra of the sample were mostly zero, with several exceptions due to noise, as depicted in Fig. S2. This result is consistent with the fact that the sample was a solution that exhibited no LD. The assumption that it might be an LD artifact when measuring CD does not hold. Our analysis confirms that CD does not possess an artifact by determining that the sample crystals exhibit no LD. The corresponding UV absorption spectra (Fig. 2e) show a broadband UV characteristic with strong UV absorption peaks caused by π- π* inter-ligand

transitions. Transitions between intermetallic and metal cause the absorption peaks in the visible area to ligand and metal charge transfer [22,23]. The inserted graph is the Tauc plot, which indicates the optical band gap of 1.9 eV. The CMOF and ligand emission spectra are shown in Figs. S3a and b, which describe the broadband emission. PL spectra of the CMOF are depicted in Fig. 2f under irradiation of 405 nm LCPL and RCPL, respectively. The measured anisotropy factor (g_{lum}) was estimated by using Equation (1).

$$g_{lum} = 2 \times (I_L - I_R) / (I_L + I_R) \quad (1)$$

I_L and I_R are the left and right CPL intensities of CMOF at 600 nm, which are about 8.3×10^{-2}. The observed g_{lum} value is comparable with the recently reported CMOFs and much greater than other reported ones [24–27]. MOFs CPL is often achieved by adding chiral ligands as guests or chiral ligands on the surface of the MOFs [24,28]. To further check the purity of CPL, a quarter-wave plate is used to convert the circular polarization to linear polarization, and a linear polarizer is placed in front of the spectrometer. Fig. S4, Supplementary Information depicts the fluorescence intensity of a single-crystal CMOF as a function of the rotational angle of the polarizer. The relationship between the maximum fluorescence intensity and the rotating angle was recorded by fixing the fast axis of the λ/4 wave plate and rotating the linear polarizer in front of a spectrometer with a step of 10^0. The high contrast of fluorescence intensities between the maximum and minimum values with a 90-degree difference indicates the CMOF is CPL-active [29].

To investigate the atomic-level electronic characteristics of CMOF, we performed *ab initio* electronic structure calculations based on the density functional theory (DFT) with the generalized gradient approximation (GGA) [30] (see the Experimental Section for the computational details). Fig. 3a shows the band structure of CMOF, where both the minimum of the valence band (MVB) and the maximum of the conduction band (MCB) are seen near the Γ point of the Brillouin zone, showing that the CMOF compound has a direct bandgap of around 1.7 eV, which is consistent with the white emission of CMOF seen in the PL experiment. This finding implies that the CMOF can be considered as a semiconductor with a modest bandgap. The calculated density of states (DOS) and projected density of states (PDOS) were shown as different colored lines in Fig. 3b. The PDOS indicates that carbon atom states dominate the valence band maximum (VBM) and conduction band minimum (CBM) around the Fermi energy level, and oxygen and nitrogen atom states make negligible contributions. Iso-surfaces of the band-decomposed partial charge density of CMOF were also displayed in Fig. 3c and d to understand band-edge features around the Fermi level. At the Fermi level, charge carrier holes (Fig. c) and electrons (Fig. d) disperse primarily across the C atoms of achiral organic ligands in CMOF, with some dispersion around the O and N atoms. The CMOF exhibits absorption peaks around UV and visible region (Fig. 2e), which can be attributed to the metal-to-ligand charge transfer (MLCT) as the HOMOs are positioned chiefly on the Sr ions (metal component). At the same time, the LUMOs are predominantly the ligand-based π* orbitals from DFTB calculations (Fig. 3c and d). The MVB and MCB are mostly made up of ligand orbitals, with a minor involvement from metals. Sr atoms contribute significantly to both the lower valence and upper conduction bands (Fig. 3b), demonstrating that Sr nodes are crucial in the electronic structure of this CMOF. The lack of a local inversion centre creates a dominating intensity in the *f-f* transitions. Based on the crystal structure, the transition intensity can demonstrate the development of a chiral environment surrounding the Sr-ions inside the complex CMOF [18].

High-performance spin optoelectronic devices are requisite for practical applications based on the excellent semiconducting physical features as described above. Consequently, the optoelectronic characteristics of the CMOF have been examined to assess its potential for the enhanced CPL detection because photodetector is one of the most important key components in the applications of optoelectronic devices. We then fabricated a spin photodetector based on the synthesized chiral MOF to evaluate its capacity. Our device's schematic design and experimental set-up are shown in Fig. 4a. The schematic construction and real images of the devices are depicted in Fig. S5. We first examined the primary performance of the photodetector on a Si/SiO_2 substrate. The CMOF active layer was spin-coated from an ethanol solution (The fabrication steps are depicted in Scheme 1), and single-layer graphene (SLG) was synthesized through chemical vapors deposition (CVD) and electrically measured under ambient conditions.

The cross-section SEM picture reveals that the spin-coated CMOF film thickness is around ≈130 nm (Fig. S6), which is the optimized thickness for the ideal device performance. The Raman spectrum (Fig. 4b) demonstrates the SLG's quality, which has a 2D/G peak intensity ratio of 2.6. The presence of high-quality graphene is confirmed by the D band's peak value, which is significantly lower than the G band; the Lorentz curve may fit the 2D peak well [31]. A laser (405 nm), a linear polarizer, and a λ/4 were used to generate CPL (Fig. 4a). The spin photodetector shows a significant difference in the photocurrent between LCPL and RCPL illumination under 405 nm with an intensity of 0.15 μw/cm^2. Fig. 4c shows that the photocurrent under LCPL illumination is more significant than that achieved from RCPL illumination of the same intensity, exhibiting a prominently specific ability between LCPL and RCPL photons. The greater photoresponse of CMOF to LCPL is presumably attributed to the higher free carrier generation efficiency in the chiral active layer triggered by spin-electron induced by LCPL absorption [18,32]. The calculated anisotropy factor (g_{lph}) (Fig. 4c) for the photocurrent is 0.38, which exceeds all the values reported for chiral MOFs. The photocurrent response of the spin photodetector under 405 nm illumination of LCPL and RCPL with 0.15 μw/cm^2 at a fixed bias of 0.1 V is depicted in Fig. 4d. The response time, i.e., on/off time, is < 200 ms, as shown in Fig. 4e. The photoresponsivity (R_{ph}), detectivity (D*), and photogain (η) are three important parameters to justify the performance of a photodetector, which were extracted using Equations (2)–(4).

$$R_{ph} = \frac{J_{ph}}{P_{light}} \quad (2)$$

$$D^* = \frac{(S\Delta f)^{1/2}}{I_n} \quad (3)$$

$$\eta = \frac{Rph}{e\lambda} \quad (4)$$

where the photocurrent density is Jph, and the power density under the illumination of LCPL and RCPL is $P_{light.}$ The maximum R_{ph}, η, and D* of CMOFs were 6.0×10^5 (A/W), $1.8 \times 10^{6,}$ and 1.83×10^{12} jones, respectively, under a bias of 0.1 V and 405 nm irradiation, as shown in Fig. 4f, g, and h. The resulting D* and R_{ph} are much higher than the recently reported heterochiral MOFs-based photodetector [19]. In particular, the photoresponsivity is more than five orders of magnitude higher than the published reports, which can be attributed to the effect of photogenerated charge carrier transfer from CMOF to the graphene layer, and the graphene layer serves as the conduction channel with a much higher carrier mobility than that of organic compounds. The performance of various devices for the investigation in this study are summaries in Table S2, which shows a negligible difference in their performance.

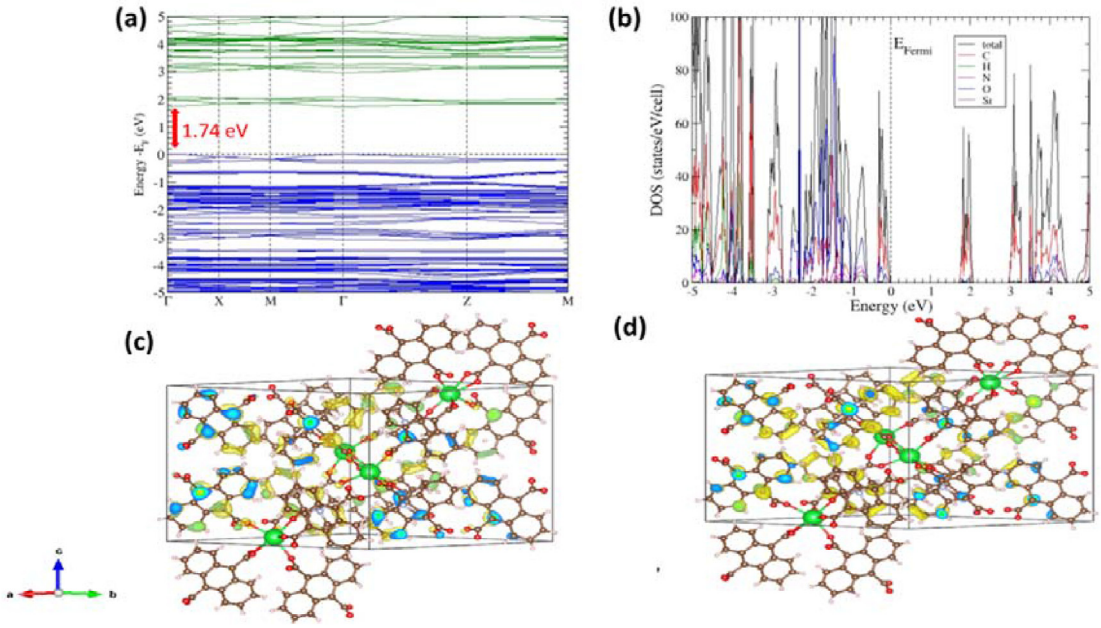

Fig. 3. DFT analysis of CMOF. (a) Direct band structure. (b) Electronic structure (DOS), dashed line shows the Fermi energy level. (c, d) Wave Function Squared distribution for VBM, and CBM at point Γ, respectively.

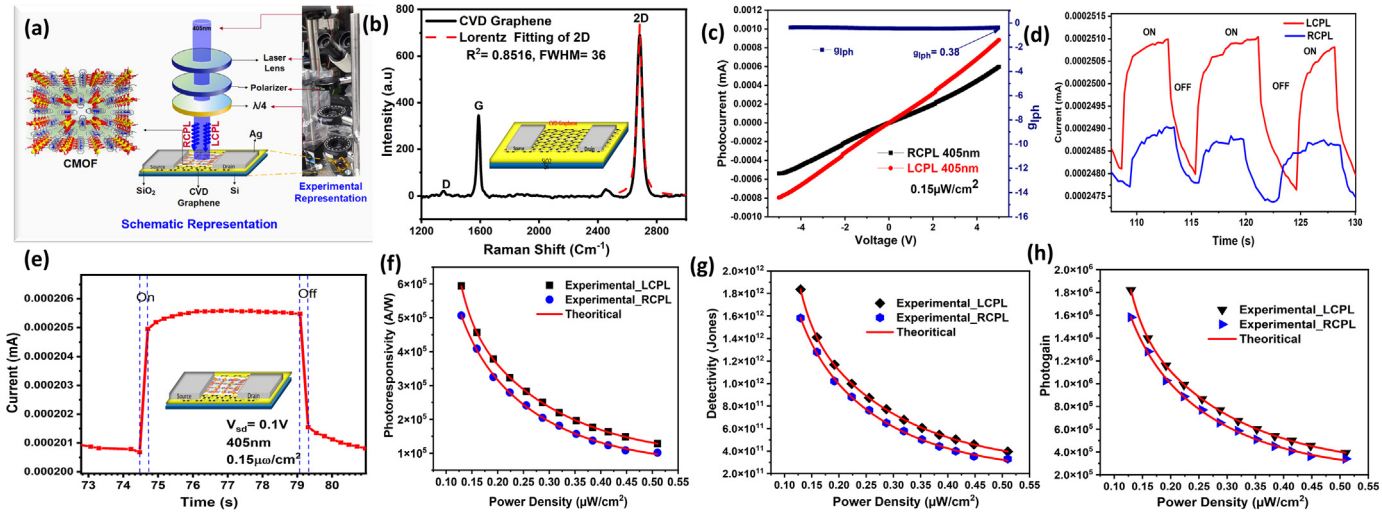

Fig. 4. (a) Illustration of the schematic and experimental set-up. (b) Raman Spectra of CVD SLG. (c) I–V characteristics of the CMOF-based spin photodetector under RCP and LCP illumination at 405 nm with an intensity of 0.15 μW/cm^2 and the calculated g_{Iph}. (d)The I-T cycle under LCPL and RCPL 405 nm illumination with the 0.15 μW/cm^2 intensity and 0.1 V bias. (e) The response time (on/off) of the device. (f, g, h) Photoresponsivity, detectivity, and photogain were calculated under the illumination of 405 nm at 0.1 V bias. The black and blue spheres resemble the experimental data, while the solid red line indicates the theoretical plot with the best fitting of the experimental data.

Furthermore, in order to confirm the underlying origin of the significant difference in the photoresponse under LCPL and RCPL illumination, grazing-incidence wide-angle X-ray scattering (GIWAXS) analysis was also conducted to investigate the crystallinity and orientation of CMOF film (Fig. 5a and b). The GIWAXS patterns of the film indicate relatively high crystallites. Evidently, there is a Debye ring of intensity for the (020) reflection, showing various potential orientations. However, the intensity for the out-of-plane is certainly quite strong compared to the in-plane condition. These findings are in agreement with the out-of-plan preferred orientation (020), which provides a good evidence for the asymmetric photoresponse in between LCPL and RCPL illumination [33]. In addition, the charge carrier lifetime (τ) was determined in order to evaluate the carrier transport parameters of the CMOF using time-resolved PL (TRPL). The PL decay traces under 374 nm excitation match the bi-exponential decay model with τ_{av} = 1.04 ns(Fig. 5c), suggesting a longer photocarrier lifetime compared with published reports [34]. CMOF's low defect charge trap density and extended carrier lifespan show that charge transport efficiency has been successfully increased in high-quality and crystalline structures [34], favourable for attaining high-performance CPL detection.

Because all the constituent materials consisted in our designed device are bendable, let us now examine the possibility of making a flexible spin photodetector. A flexible CMOF-based spin photodetector was fabricated on a PET substrate, as depicted in Fig. 6a.

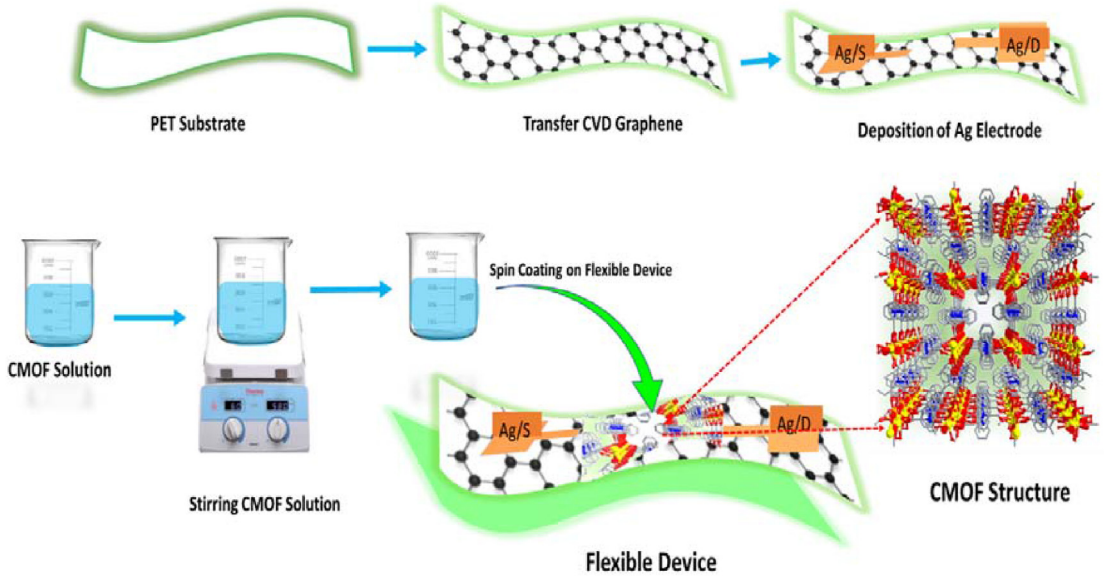

Scheme 1. Fabrication steps of the spin photodetector.

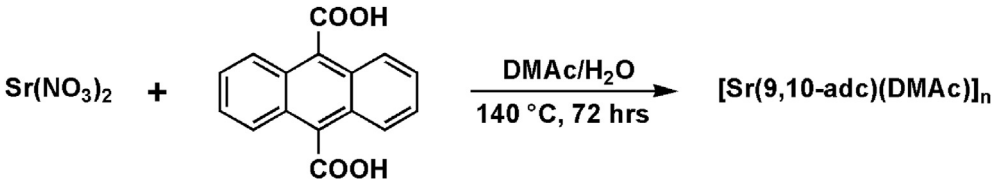

Scheme 2. Synthesis of chiral MOF.

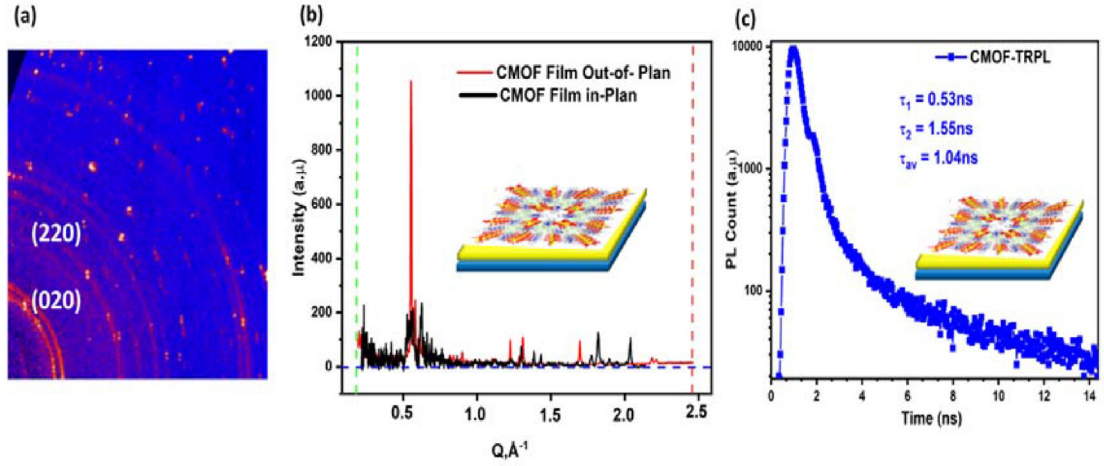

Fig. 5. (a) GIWAX pattern, (b) (red line) CMOF Film "Out-of-plane"; (black line) CMOF Film "in-plane". (c) TRPL spectra of CMOF. The PL τ are calculated via biexponential fitting.

When the device is exposed to LCPL and RCPL illumination with 405 nm and 0.15 μw/cm^2, a distinct photocurrent is obtained, as shown in Fig. 6b, which indicates a strong CPL distinguishability. The resulting anisotropic photocurrent factor, g_{lph}, was determined to be 0.14 at 0.1 V bias, indicating a suitable material for CPL detection. In order to further explore the constraints of the anisotropic photocurrent factor (g_{lph}), we adjusted the light intensity and the thickness of the chiral active layer. A slightly decreasing of g_{lph} was also influenced by the thickness of the active layer, possibly because of the reduced contribution of chiral enhancement to the thickness of the active layer. The effect of light intensity and thickness of a chiral active layer on g_{lph} factor indicates that the photocurrent is mainly generated from the photo-induced carriers in the chiral active layer. For the current study, we used ≈130 nm, which is the optimized thickness for the ideal device performance [35–37]. Furthermore, the flexible device's maximum responsivity (R), photogain, and detectivity (D*), 9.4 × 10^3 (A/W), 2.8 × 10^4, and 9.1 × 10^{10} jones were obtained (Fig. 6c, d and e). Compared with the

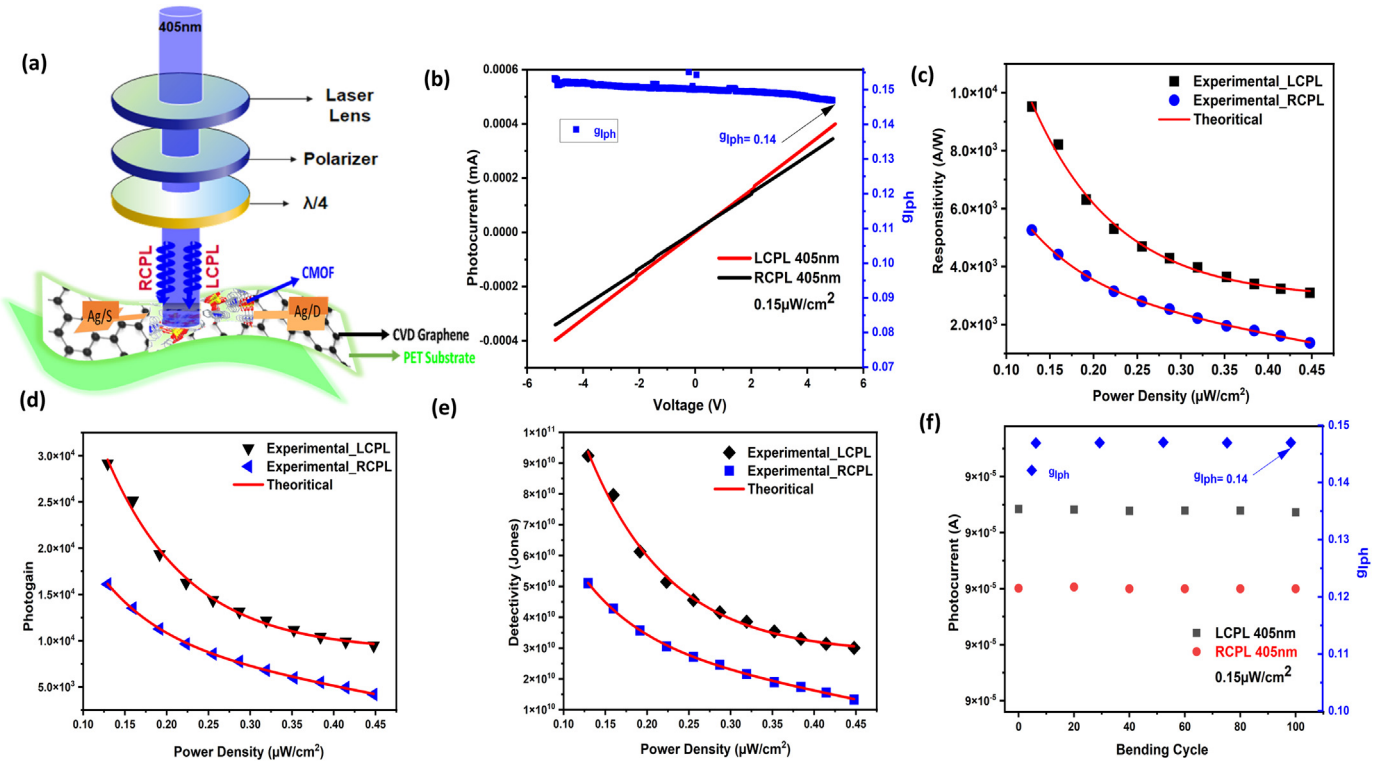

Fig. 6. (a) The illustration of a flexible spin photodetector based on CMOF. (b) I–V characteristics of the flexible spin photodetector under the illumination of RCP and LCP at 405 nm with an intensity of 0.15 μW/cm^2 and the calculated g_{lph}. (c,d,e) Photoresponsivity, photogain, and detectivity were calculated under the illumination of 405 nm at 0.1 V bias. (f) Bending cycles under various bending curvatures and g_{lph}.

device based on Si/SiO_2 substrate, the performance of the device shows a degradation, when it is deposited on PET substrate. This behaviour can be attributed to the inherent rough surface of the PET. It is because the rough surface of the PET substrate can introduce disorder arrangement of the CMOF molecules. The flexible spin photodetector's mechanical flexibility was evaluated via bending tests at various curvatures. The associated photocurrent stays constant at varying curvature radii, as illustrated in Fig. S7, demonstrating outstanding device stability. Fig. 6f depicts the ability of a flexible thin-film spin photodetector to detect CPL under repeated bending/straightening tests. After 100 cycles of bending, photocurrent and g_{lph} exhibited a slight deterioration, showing the minor effect of external bending force on the device performance (Fig. 6f). These findings represent a valuable step toward developing CMOF based flexible spin photodetector systems capable of serving as wearable devices.

3. Conclusions

In summary, we have developed CMOF based on achiral building blocks and demonstrated their excellent capability for the application in spin photodetection. The CMOF crystals exhibit a non-centrosymmetric chiral space group (*I -4 2 d*) and high crystalline quality, as shown by X-ray spectra. The fabricated CMOF film has intrinsic chirality and can emit and distinguish CPL photons. The underlying origin can be understood well by the intense SHG activity and the GIWAXS patterns of the film with the out-of-plan preferred orientation along (020), which provides a good evidence for the asymmetric photoresponse in between LCPL and RCPL illumination. The resulting spin photodetector based on CMOF/graphene heterostructure exhibited outstanding chirality with a high g_{lph} of 0.38 under 0.1 V bias. An excellent detectivity of 1.83×10^{12} jones and photoresponsivity of 6.0×10^5 (A/W) were also obtained, and both are the highest values ever reported for heterochiral MOFs-based detectors. Additionally, we demonstrated a flexible spin photodetector with outstanding endurance, making it a suitable choice for implementation in wearable devices. Our findings are, therefore, very useful in providing an alternative route for developing spin optoelectronic devices based on CMOFs, which can have a wide range of applications spanning from optical communication to pharmaceutical synthesis.

4. Experimental Section

4.1. Synthesis of [Sr (9,10-adc) $(DMAc)_2]_n$

Sr $(NO_3)_2$ (21.8 mg, 0.1 mmol), 9,10-anthracene dicarboxylic acid (26.6 mg, 0.1 mmol), dimethylacetamide (5 mL), and H_2O (2 mL) were sealed in a Teflon-lined stainless-steel Parr acid digestion bomb and heated at 140 °C for 72 h and then allowed to cool at a rate of 6 h/°C (Scheme 2). Colorless rectangular-shaped crystals of CMOF were obtained in a 43.6% yield. The solids were collected using a filter, rinsed in water, and dried at room temperature. Elementary anal. Calcd (%); C, 55.88; H, 1.88; N, 3.26. Found (%): C, 55.09; H, 4.1; N, 3.25. IR data (KBr, cm^{-1}): 3681(w), 2810 (w), 2553 (s), 1682 (s), 1424 (s), 1189(s), (w), 1916(m), 835(w), 751(s), 639 (w), 560 (s), 481(s).

5. Growth of SLG

High-quality single-layer graphene (SLG) was developed using the CVD process on Cu foil.[42] To lessen surface roughness, the Cu foil was cleaned by electrolysis with 85% H_3PO_4 at 1.7 V for 20 min.

Finally, as we already reported [38], the cleaned Cu was used to create high-quality graphene in a CVD furnace.

6. Device fabrication

6.1. Spin photodetector on SiO_2 substrate

The wafers utilized were Si/SiO_2 wafers (CCMS, Physics Institute), which had a p-type Si material with 300 nm wet thermal oxide SiO_2. These substrates were cleaned ultrasonically for 30 min in acetone and isopropyl alcohol and then dried using nitrogen gas. After transferring the SLG, the wafer was patterned with thermally deposited Ag electrodes. At 3000 rpm, the CMOF solution was spin-coated onto the substrate (Scheme 1). All samples and devices were prepared under ambient (N_2 environment) conditions.

6.2. Spin photodetector on flexible (PET) substrate

A PET substrate was cleaned using the same process as before; SLG was transferred onto the substrate after cleaning. The designed Ag source and drain electrodes were thermally $\approx$ 100 nm with shadow masks. Lastly, the CMOF solution was spin-coated onto the device.

6.3. Characterization

A Brucker-Nonius Kappa CCD diffractometer with graphite-monochromated Mo K radiation ($\lambda = 0.7107$) was used to measure CMOF diffraction. The crystallographic data collection parameters for compound 1 are listed in Table S1 (ESI). Structural refinement was performed using direct methods and the SHELXL-97 program, full-matrix least-squares on F^2 values. All non-hydrogen atoms were refined anisotropically, while the hydrogen atoms were placed in ideal and calculated positions, with isotropic thermal parameters riding on their respective carbon atoms. Thermogravimetric (TG) analyses were done under nitrogen with a heating rate of 10 °C min^{-1} on a Perkin-Elmer TGA-7 TG analyzer. Powder diffraction studies were examined using a Siemens D-5000 diffractometer at 40 kV, 30 mA for Cu Kα ($\lambda = 1.5406$ Å), with a step size of 0.015 and a scan speed of 0.15 s per step. Using Kurtz- Perry's method, The NLO properties of CMOF were examined on a LeCroy WR64xi digital oscilloscope. Electronic device measurements were performed using a Keithley 2400 under ambient (N_2 environment) conditions. The CPL effect of the device was tested under a He-Cd laser of 405 nm wavelength with a density filter, quarter-wave plate, and linear polarizer. FEI Helios NanoLab 660 Dual Beam FESEM/FIB system was used to obtain FESEM images.

6.4. Ab initio electronic structure calculation

To help understand the intriguing experimental results, we perform *ab initio* electronic structure calculations for the COMF. The present calculations are based on the density functional theory with the generalized gradient approximation [30]. The accurate projector-augmented wave method, as implemented in the VASP package [39,40], is used. A large plane wave cutoff energy of 450 eV is used. The self-consistent electronic structure calculations are performed with a k-point grid of $4 \times 4 \times 4$. The obtained energy bands along the high symmetry lines in the Brillouin zone as well as the total and atom-decomposed density of states (DOSs), are displayed in Fig. 3a and b, respectively.

Declaration of competing interest

The authors declare that they have no known competing financial interests or personal relationships that could have appeared to influence the work reported in this paper.

Data availability

Data will be made available on request.

Acknowledgments

This work was financially supported by the "Advanced Research Centre for Green Materials Science and Technology" from the Featured Area Research Centre Program within the framework of the Higher Education Sprout Project by the Ministry of Education (111L9006) and the National Science and Technology Council in Taiwan (NSTC111-2634-F-002 -016, NSTC 110-2112-*M*-002-044). The author would like to acknowledge the Taiwan International Graduate Program (TIGP), Institute of Physics, Academia Sinica, and Department of Physics, National Taiwan University, Taipei, Taiwan, for their constant support.

Author contributions

Y·F·C provided the idea, supervised the project and conceived the study. M.M and S·K equally contribute, designed the material, device and developed the fabrication methods, performed the time-response measurements, analyzed the data and wrote the manuscript. N.A carried out the SEM and EDX characterization. P.T.C discussed the results and comments on the manuscript. K.H.L and H·C·Y performed the CPL and UV−Vis measurements. Y.C.H performed the GIWX analysis. G.Y.G and W.K.L done the DFT calculations. C.R.P.I supporting in IV measurements K.L.L and Y.F.C discussed the results and comments on the manuscript. All authors accepted the final version of the manuscript.

Appendix A. Supplementary data

Supplementary data to this article can be found online at https://doi.org/10.1016/j.mtnano.2023.100303.

References

[1] W.B. Sparks, T.A. Germer, R.M. Sparks, Classical polarimetry with a twist: a compact, geometric approach, PASP 131 (2019), 075002, https://doi.org/10.1088/1538-3873/ab1933.
[2] Experimental demonstration of memory-enhanced quantum communication, Nature 580 (2020) 60, https://doi.org/10.1038/s41586-020-2103-5.
[3] C. Zhang, X. Wang, L. Qiu, Circularly polarized photodetectors based on chiral materials: a review, Front. Chem. 9 (2021), 711488, https://doi.org/10.3389/fchem.2021.711488.
[4] Y.-P. Xue, C.-H. Cao, Y.-G. Zheng, Enzymatic asymmetric synthesis of chiral amino acids, Chem. Soc. Rev. 47 (2018) 1516, https://doi.org/10.1039/C7CS00253J.
[5] X. Kou, Q. Shao, C. Ye, G. Yang, W. Zhang, Asymmetric Aza-Wacker-type cyclization of N-Ts hydrazine-tethered tetrasubstituted olefins: synthesis of pyrazolines bearing one quaternary or two vicinal stereocenters, JACS 140 (2018) 7587, https://doi.org/10.1021/jacs.8b02865.
[6] L. Wang, Q. Li, Photochromism into nanosystems: towards lighting up the future nanoworld, Chem. Soc. Rev. 47 (2018) 1044, https://doi.org/10.1039/C7CS00630F.
[7] F. Pop, N. Zigon, N. Avarvari, Main-group-based electro-and photoactive chiral materials, Chem. Rev. 119 (2019) 8435, https://doi.org/10.1021/acs.chemrev.8b00770.
[8] F. Zinna, G. Albano, A. Taddeucci, T. Colli, L.A. Aronica, G. Pescitelli, L. Di Bari, Emergent nonreciprocal circularly polarized emission from an organic thin film, Adv. Mater. 32 (2020), 2002575, https://doi.org/10.1002/adma.202002575.

[9] L.E. MacKenzie, R. Pal, Circularly polarized lanthanide luminescence for advanced security inks, Nat. Rev. Chem 5 (2021) 109, https://doi.org/10.1038/s41570-020-00235-4.
[10] C. He, Z. Feng, S. Shan, M. Wang, X. Chen, G. Zou, Highly enantioselective photo-polymerization enhanced by chiral nanoparticles and in situ photo-patterning of chirality, Nat. Commun. 11 (2020) 1, https://doi.org/10.1038/s41467-020-15082-6.
[11] S. Ma, J. Ahn, J. Moon, Chiral perovskites for next-generation photonics: from chirality transfer to chiroptical activity, Adv. Mater. 33 (2021), 2005760, https://doi.org/10.1002/adma.202005760.
[12] M. Schulz, F. Balzer, D. Scheunemann, O. Arteaga, A. Lützen, S.C. Meskers, M. Schiek, Chiral excitonic organic photodiodes for direct detection of circular polarized light, Adv. Funct. Mater. 29 (2019), 1900684, https://doi.org/10.1002/adfm.201900684.
[13] W. Gong, W. Zhang, F.A. Son, K. Yang, Z. Chen, X. Chen, J. Jiang, Y. Liu, O.K. Farha, Y. Cui, Topological strain-induced regioselective linker elimination in a chiral Zr (IV)-based metal-organic framework, Chem 7 (2021) 190, https://doi.org/10.1016/j.chempr.2020.11.008.
[14] D. Wu, K. Zhou, J. Tian, C. Liu, J. Tian, F. Jiang, D. Yuan, J. Zhang, Q. Chen, M. Hong, Induction of chirality in a metal−organic framework built from achiral precursors, Angew. Chem. 133 (2021) 3124, https://doi.org/10.1002/ange.202013885.
[15] H. Jiang, W. Zhang, X. Kang, Z. Cao, X. Chen, Y. Liu, Y. Cui, Topology-based functionalization of robust chiral Zr-based metal−organic frameworks for catalytic enantioselective hydrogenation, JACS 142 (2020) 9642, https://doi.org/10.1021/jacs.0c00637.
[16] X. Li, J. Wu, C. He, Q. Meng, C. Duan, Asymmetric catalysis within the chiral confined space of metal−organic architectures, Small 15 (2019), 1804770, https://doi.org/10.1002/smll.201804770.
[17] W. Shang, X. Zhu, T. Liang, C. Du, L. Hu, T. Li, M. Liu, Chiral reticular self-assembly of achiral AIEgen into optically pure metal−organic frameworks (MOFs) with dual mechano-switchable circularly polarized luminescence, Angew. Chem. Int. Ed. 59 (2020), 12811, https://doi.org/10.1002/anie.202005703.
[18] Z. Sharifzadeh, K. Berijani, A. Morsali, Chiral metal−organic frameworks based on asymmetric synthetic strategies and applications, Coord. Chem. Rev. 445 (2021), 214083, https://doi.org/10.1016/j.ccr.2021.214083.
[19] X. Shang, I. Song, G.Y. Jung, W. Choi, H. Ohtsu, J.H. Lee, J. Ahn, J.Y. Koo, M. Kawano, S.K. Kwak, Micro-/nano-sized multifunctional heterochiral metal−organic frameworks for high-performance visible−blind UV photodetectors, J. Mater. Chem. C 9 (2021) 7310, https://doi.org/10.1039/D1TC01333E.
[20] H.-P. Wang, S.-Y. Yin, M. Pan, K. Wu, L. Chen, Y.-X. Zhu, Y.-J. Hou, Circular dichroism enhancement by the coordination of different metal ions with a pair of chiral tripodal ligands, Inorg. Chem. Commun. 54 (2015) 92, https://doi.org/10.1016/j.inoche.2015.02.013.
[21] H. Satozono, Measurement of circular dichroism spectra without control of a phase modulator using retardation domain analysis, Molecules 24 (2019) 1418. https://www.mdpi.com/1420-3049/24/7/1418.
[22] L. Zou, D. Feng, T.-F. Liu, Y.-P. Chen, S. Yuan, K. Wang, X. Wang, S. Fordham, H.-C. Zhou, A versatile synthetic route for the preparation of titanium metal−organic frameworks, Chem. Sci. 7 (2016) 1063, https://doi.org/10.1039/C5SC03620H.
[23] F. Song, W. Li, Y. Sun, Metal−organic frameworks and their derivatives for photocatalytic water splitting, INORGA 5 (2017) 40, https://doi.org/10.3390/inorganics5030040.
[24] T. Zhao, J. Han, X. Jin, Y. Liu, M. Liu, P. Duan, Enhanced circularly polarized luminescence from reorganized chiral emitters on the skeleton of a zeolitic imidazolate framework, Angew. Chem. 131 (2019) 5032, https://doi.org/10.1002/ange.201900052.
[25] S.-M. Chen, L.-M. Chang, X.-K. Yang, T. Luo, H. Xu, Z.-G. Gu, J. Zhang, Liquid-phase epitaxial growth of azapyrene-based chiral metal−organic framework thin films for circularly polarized luminescence, ACS Appl. Mater. Interfaces 11 (2019), 31421, https://doi.org/10.1021/acsami.9b11872.
[26] T. Zhao, J. Han, X. Jin, M. Zhou, Y. Liu, P. Duan, M. Liu, Dual-mode induction of tunable circularly polarized luminescence from chiral metal-organic frameworks, Research (2020), https://doi.org/10.34133/2020/6452123, 2020.
[27] C. Zhang, Z.P. Yan, X.Y. Dong, Z. Han, S. Li, T. Fu, Y.Y. Zhu, Y.X. Zheng, Y.Y. Niu, S.Q. Zang, Enantiomeric MOF crystals using helical channels as palettes with bright white circularly polarized luminescence, Adv. Mater. 32 (2020), 2002914, https://doi.org/10.1002/adma.202002914.
[28] L. Hu, K. Li, W. Shang, X. Zhu, M. Liu, Emerging cubic chirality in γcd-MOF for fabricating circularly polarized luminescent crystalline materials and the size effect, Angew. Chem. 132 (2020) 4983, https://doi.org/10.1002/ange.202000589.
[29] X.-Z. Wang, M.-Y. Sun, Z. Huang, M. Xie, R. Huang, H. Lu, Z. Zhao, X.-P. Zhou, D. Li, Turn-on circularly polarized luminescence in metal−organic frameworks, Adv. Opt. Mater. 9 (2021), 2002096, https://doi.org/10.1002/adom.202002096.
[30] J.P. Perdew, K. Burke, M. Ernzerhof, Generalized gradient approximation made simple, Phys. Rev. Lett. 77 (1996) 3865, https://doi.org/10.1103/PhysRevLett.77.3865.
[31] X. Li, W. Cai, J. An, S. Kim, J. Nah, D. Yang, R. Piner, A. Velamakanni, I. Jung, E. Tutuc, Large-area synthesis of high-quality and uniform graphene films on copper foils, science 324 (2009) 1312, https://doi.org/10.1016/j.cej.2021.131079.
[32] C. Chen, L. Gao, W. Gao, C. Ge, X. Du, Z. Li, Y. Yang, G. Niu, J. Tang, Circularly polarized light detection using chiral hybrid perovskite, Nat. Commun. 10 (2019) 1, https://doi.org/10.1038/s41467-019-09942-z:.
[33] L.N. Appelhans, L. Hughes, B. McKenzie, M. Rodriguez, J. Griego, J. Briscoe, M. Moorman, E. Frederick, J.B. Wright, Facile microwave synthesis of zirconium metal-organic framework thin films on gold and silicon and application to sensor functionalization, Microporous Mesoporous Mater. 323 (2021), 111133, https://doi.org/10.1016/j.micromeso.2021.111133.
[34] J. Ji, B. Liu, H. Huang, X. Wang, L. Yan, S. Qu, X. Liu, H. Jiang, M. Duan, Y. Li, Nondestructive passivation of the TiO 2 electron transport layer in perovskite solar cells by the PEIE-2D MOF interfacial modified layer, J. Mater. Chem. C 9 (2021) 7057, https://doi.org/10.1039/D1TC00036E.
[35] H. Kim, R.M. Kim, S.D. Namgung, N.H. Cho, J.B. Son, K. Bang, M. Choi, S.K. Kim, K.T. Nam, J.W. Lee, Ultrasensitive near-infrared circularly polarized light detection using 3D perovskite embedded with chiral plasmonic nanoparticles, Adv. Sci. 9 (2022), 2104598, https://doi.org/10.1002/advs.202104598.
[36] L. Wang, Y. Xue, M. Cui, Y. Huang, H. Xu, C. Qin, J. Yang, H. Dai, M. Yuan, A chiral reduced-dimension perovskite for an efficient flexible circularly polarized light photodetector, Angew. Chem. 132 (2020) 6504, https://doi.org/10.1002/ange.201915912.
[37] D. Zhu, W. Jiang, Z. Ma, J. Feng, X. Zhan, C. Lu, J. Liu, J. Liu, Y. Hu, D. Wang, Y.S. Zhao, J. Wang, Z. Wang, L. Jiang, Organic donor-acceptor heterojunctions for high performance circularly polarized light detection, Nat. Commun. 13 (2022) 3454, https://doi.org/10.1038/s41467-022-31186-7.
[38] M. Mustaqeem, J.-Y. Lin, S. Kamal, A. Thakran, G.-Z. Lu, G. Naikoo, P.-T. Chou, K.-L. Lu, Y.-F. Chen, Optically encodable and erasable multilevel nonvolatile flexible memory device based on metal−organic frameworks, ACS Appl. Mater. Interfaces (2022), https://doi.org/10.1021/acsami.2c02440.
[39] G. Kresse, J. Hafner, Ab initio molecular dynamics for liquid metals, Phys. Rev. B 47 (1993) 558, https://doi.org/10.1103/PhysRevB.47.558.
[40] G. Kresse, J. Furthmüller, Efficiency of ab-initio total energy calculations for metals and semiconductors using a plane-wave basis set, Comput. Mater. Sci. 6 (1996) 15, https://doi.org/10.1016/0927-0256(96)00008-0.